Large second-harmonic generation and linear electro-optic effect in trigonal selenium and tellurium

Meijuan Cheng,[1] Shunqing Wu,[1] Zi-Zhong Zhu,[1,2,*] and Guang-Yu Guo[3,4,†]

[1]*Department of Physics, Collaborative Innovation Center for Optoelectronic Semiconductors and Efficient Devices, Key Laboratory of Low Dimensional Condensed Matter Physics (Department of Education of Fujian Province), Jiujiang Research Institute, Xiamen University, Xiamen 361005, China*

[2]*Fujian Provincial Key Laboratory of Theoretical and Computational Chemistry, Xiamen 361005, China*

[3]*Department of Physics and Center for Theoretical Physics, National Taiwan University, Taipei 10617, Taiwan*

[4]*Physics Division, National Center for Theoretical Sciences, Hsinchu 30013, Taiwan*

(Received 2 April 2019; revised manuscript received 20 June 2019; published 11 July 2019)

Trigonal selenium and tellurium crystalize in helical chainlike structures and thus possess interesting properties such as nontrivial band topology, gyrotropic effects, and nonlinear optical responses. By performing systematic density-functional-theory calculations with the generalized gradient approximation plus scissors correction, we study their linear and nonlinear optical (NLO) properties. We find that both materials exhibit large second-harmonic generation (SHG) and linear electro-optic (LEO) effect. In particular, tellurium has the huge SHG coefficient ($\chi^{(2)}_{xxx}$) in the photon energy range of $0 \sim 3$ eV with the maximum magnitude being about 16 times larger than that of GaN, a widely used NLO material. Tellurium is also found to possess the gigantic static SHG coefficient $\chi^{(2)}_{xyz}$, which is up to 100 times larger than that of GaN. On the other hand, selenium exhibits the large LEO coefficient $r_{xxx}(0)$, which is more than six times larger than that of GaN. Thus, tellurium and selenium may find valuable applications in NLO and LEO devices such as frequency conversion, electro-optical switches, and light signal modulators. Interestingly, our calculations also reveal that for each material, the $\chi^{(2)}_{xxx}$ values for the two helical structures are equal but the $\chi^{(2)}_{xyz}$ values differ in sign, suggesting that the SHG spectroscopy is a useful probe of their chirality. The calculated static and optical dielectric constants as well as SHG coefficients at the CO_2 laser frequency are in good agreement with the available experiments. Finally, much stronger NLO responses of selenium and tellurium compared with the semiconductors with similar band gaps are attributed to their quasi-one-dimensional structures with directional covalent bonding and lone-pair electrons. These findings will help the search for new materials with large NLO coefficients.

DOI: 10.1103/PhysRevB.100.035202

I. INTRODUCTION

The interaction between intense optical fields and materials may induce strong nonlinear optical (NLO) responses [1,2]. Noncentrosymmetric materials with large second-order NLO susceptibility ($\chi^{(2)}$) play a crucial role in the development of modern optical and electro-optical devices such as lasers, frequency conversions, electro-optic modulators, and switches [2]. Second-harmonic generation (SHG), a special case of sum frequency generation, is perhaps the best-known NLO effect. Since the 1960s, the SHG has been investigated extensively in bulk semiconductors [2–7] and more recently also in one-dimensional (see, e.g., Refs. [8,9] and references therein) and two-dimensional (see, e.g., Refs. [10–13] and references therein) materials. Furthermore, because of its high sensitivity to local structure symmetry, the SHG has been a powerful probe of surfaces and interfaces [1]. Linear electro-optic (LEO) effect, another second-order electric polarization response of a NLO material, refers to the linear refractive index variation (Δn) with the applied electric field strength (E), $\Delta n = n^3 rE/2$, where n is the refraction index and r is the LEO coefficient [2]. The LEO effect thus allows one to use an electrical signal to control the amplitude, phase, or direction of a light beam in the NLO material, and leads to a widely used means for high-speed optical modulation and sensing devices (see, e.g., Ref. [14] and references therein).

Since their discovery, trigonal selenium and tellurium have attracted considerable attention due to their unique properties, such as a high degree of anisotropy, broken inversion symmetry, and chirality [15–19]. Trigonal selenium has valuable technological applications such as rectifiers, photocells, photographic exposure meters, and xerography to medical diagnostics due to their photoconductivity in the entire visible range [20–23]. As a narrow band-gap semiconductor, tellurium possesses excellent thermoelectric properties [17,24] and thus can be used for thermoelectrics. Furthermore, tellurium also exhibits such interesting behaviors as current-induced spin polarization [25], trivial insulator to strong topological insulator transition under shear strain [16], circular photon drag effect [26], robust control over current-induced magnetic torques [27], and gyrotropic effects [28]. Finally, their electronic band structures host Dirac and Weyl nodes due to the broken inversion symmetry and spin-orbit coupling (SOC) [18,19].

As semiconductors without inversion symmetry, selenium and tellurium exhibit second-order NLO responses. Although

*zzhu@xmu.edu.cn
†gyguo@phys.ntu.edu.tw

their linear optical properties [4,29–33] have been extensively studied, their NLO effects have hardly been investigated. Only the second-order NLO susceptibility element $\chi^{(2)}_{xxx}$ has been measured at the CO_2 laser frequency ($\hbar\omega = 0.113$ meV) for selenium and tellurium [29,32,33] and calculated at zero frequency for selenium [4]. No study on the other nonzero element $\chi^{(2)}_{xyz}$ has been reported. Since the SHG depends on the electronic band structure, dipole transition matrix, and specific frequency and orientation of the applied optical field, it is of interest to know all the nonzero SHG elements over the entire optical frequency range. The LEO effect in these two materials has not been investigated either. Therefore, the main objectives of this paper are as follows. First, we want to perform systematic *ab initio* calculations of all the nonzero elements of the second-order NLO susceptibility tensor $\chi^{(2)}_{\alpha\beta\gamma}(-2\omega, \omega, \omega)$ of both materials for the whole optical frequency range. The results will tell us whether trigonal selenium and tellurium are promising NLO materials for optical and opto-electronic devices. Second, we also want to calculate linear optical dielectric functions $\varepsilon(\omega)$ for both selenium and tellurium to understand the interesting observed optical phenomena. The calculated dielectric functions will also help us to understand the obtained SHG coefficients [6,9,10]. Furthermore, since a NLO material with a large LEO coefficient needs to simultaneously possess a large second-order NLO susceptibility and a low dielectric constant, the dielectric functions are also required for evaluating the LEO coefficient. Our findings are expected to stimulate further experimental investigations on the NLO properties of these interesting helical chainlike materials.

The paper is organized as follows. In Sec. II, we present the theory and computational details. In Sec. III, the calculated optical dielectric function, SHG, and LEO coefficients over the entire optical frequency range are reported. Comparison of the obtained SHG and LEO coefficients of the materials with the known NLO materials suggests that they are superior NLO materials. The theoretical SHG coefficients are compared with the measured values at the CO_2 laser frequency, and also analyzed in terms of one- and two-photon resonances via the calculated absorptive parts of the dielectric function. Moreover, we compare the calculated dielectric function over the whole optical frequency range with the available experimental results and also analyze their interesting features in terms of the symmetry of band states at high symmetry k-points in the Brillouin zone. Finally, conclusions drawn from this work are given in Sec. IV.

II. STRUCTURE AND COMPUTATIONAL METHOD

The crystal structure of trigonal selenium and tellurium [34,35] is schematically shown in Fig. 1. It consists of the helical chains arranged in a hexagonal array [34,35]. The three atoms in the unit cell are situated at positions $(u, 0, 0)$, $(0, u, 1/3)$, and $(-u, -u, 2/3)$. The space group is either $P3_121$ (D^4_3) or $P3_221$ (D^6_3), depending on whether it has the right-handed or left-handed screw. Nonetheless, the two different helical structures are related to each other by spatial inversion. Thus, their energy bands and linear optical properties should be identical. Furthermore, their nonzero elements of the second-order NLO susceptibility tensor would be the same and are also related to each other, as will be explained in Sec. III C below. Thus, we only consider the D^4_3 case here. The structures could be viewed as being derived from the Peierls distortion [36] of the six-coordinated simple cubic structure. The valence electron configurations of selenium and tellurium are $4s^24p^4$ and $5s^25p^4$, respectively, i.e., one-third of the p bands are empty. Consequently, every atom is covalently bonded to two neighboring atoms along each chain, and interacts with four second-nearest-neighbor atoms of the adjacent chains by van der Waals forces. The intrachain bonding and interchain bonding correspond to the p bonding and the lone pair states, respectively. The overlap of electronic orbitals arising from the lone pair and antibonding states on neighboring chains induces the covalent bond stretched to infinity. Furthermore, such overlap and the repellant exchange

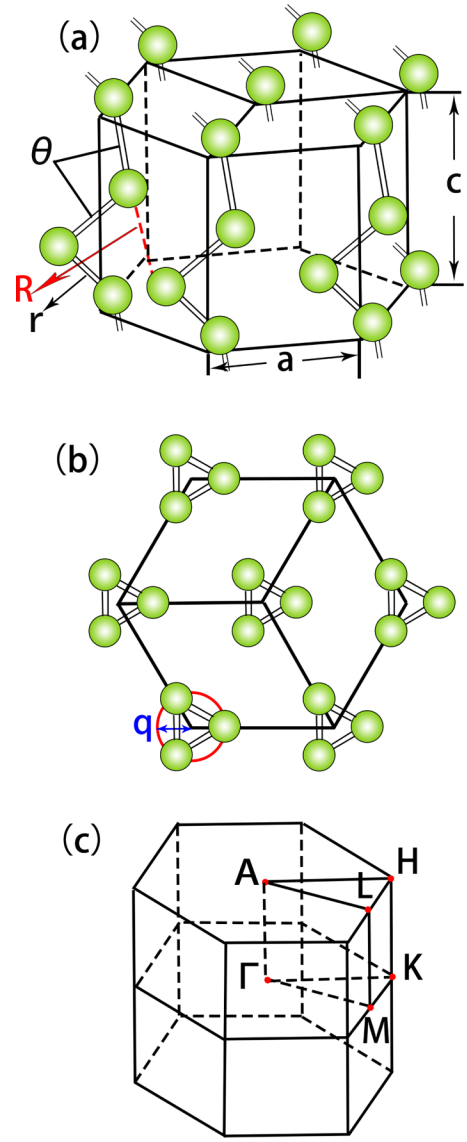

FIG. 1. (a) Side and (b) top views of the trigonal crystalline structure of selenium and tellurium as well as (c) the associated Brillouin zone. a and c are lattice constants. θ, r, and R are bond angle, intrachain, and interchain distances, respectively. q denotes the radius of the helices.

TABLE I. Calculated (the) and measured (exp) lattice constants a and c, atomic-position parameter u, the distances of intrachain r and interchain R, bond angle θ, cell volume V.

		a (Å)	c (Å)	u	r (Å)	R (Å)	$\theta(^\circ)$	V (Å^3)
Se	exp[a]	4.3662	4.9536	0.2254	2.3732	3.4358	103.07	81.78
	the	4.3084	5.0874	0.2315	2.4207	3.3958	103.66	81.78
Te	exp[b]	4.4511	5.9262	0.2633	2.8325	3.4908	103.27	101.68
	the	4.4345	5.9707	0.2754	2.9044	3.4428	101.79	101.67

[a]Ref. [34].
[b]Ref. [35].

interaction between lone pair orbitals stabilize the helical chains. As shown in Fig. 1, lattice constant a amounts to the distance between the adjacent chains. Lattice constant c is equal to the height of the unit cell in the chain direction (the c axis). Interestingly, the atomic position parameter $u = q/a$ can be related to lattice constant a and the helix radius q. Note that the ratio (R/r) of the interchain and intrachain distances of tellurium is smaller than that of selenium (Table I), implying a weaker structural anisotropy in tellurium.

The present *ab initio* calculations are performed based on the density-functional theory with the generalized gradient approximation (GGA) of Perdew, Burke, and Ernzerhof [37]. The resultant GGA lattice constants agree rather well with that of experiments (see Table I). The accurate projector-augmented wave (PAW) method [38], as implemented in the VASP package [39,40], is used. A large plane-wave cutoff ($E_{\rm cut}$) of 450 eV is adopted throughout. Test calculations using $E_{\rm cut} = 500$ eV for selenium yields the band structure being identical to that of $E_{\rm cut} = 450$ eV. The PAW potentials are used to describe the electron-ion interaction, with six valence electrons for Se ($4s^2 4p^4$) and also for Te ($5s^2 5p^4$). The theoretical atomic positions and lattice constants are fully relaxed until the forces acting on all the atoms are less than 0.01 eV/Å and the stresses are less 8.0 kBar, respectively. The total energy convergence criterion for the self-consistent electronic structure calculations is 10^{-6} eV. The accurate tetrahedron method [41] is used for the Brillouin zone integration. A k-point mesh of $10 \times 10 \times 8$ is used for the self-consistent charge density calculations. The density of states (DOS) is evaluated from the self-consistent band structure with a much denser k-point mesh of $20 \times 20 \times 18$ for Se and of $20 \times 20 \times 16$ for Te. Further calculations using different k-point meshes indicate that the above k-point meshes produce the well-converged charge density and DOS spectra, respectively.

We first perform structural optimizations of the atomic positions and lattice constants with the conjugate gradient technique. Table I shows that the calculated lattice constants agree rather well with that of experiments [34,35] except lattice constant c of selenium, which is about 2.6 % too small. Nonetheless, the calculated linear and NLO spectra using the theoretical structural parameters look almost the same as that obtained using the experimental structural parameters. Therefore, only the results calculated by using the experimental structural parameters are presented in this paper.

The optical dielectric function and NLO susceptibility are calculated based on the linear response formalism with the independent-particle approximation, as described previously [8,42]. Therefore, the imaginary part of the dielectric function $\varepsilon(\omega)$ due to direct interband transitions is given by the Fermi golden rule [8,42],

$$\varepsilon_a''(\omega) = \frac{4\pi^2}{\Omega\omega^2} \sum_{i\in \mathrm{VB}, j\in \mathrm{CB}} \sum_k w_k \left| p_{ij}^a \right|^2 \delta(\epsilon_{\mathbf{k}j} - \epsilon_{\mathbf{k}i} - \omega), \quad (1)$$

where ω is the photon energy and Ω is the unit-cell volume. VB and CB represent the valence and conduction bands, respectively. The dipole transition matrix elements $p_{ij}^a = \langle \mathbf{k}j | \hat{p}_a | \mathbf{k}i \rangle$ are obtained from the self-consistent band structures within the PAW formalism [43]. Here $|\mathbf{k}n\rangle$ is the nth Bloch state wave function with crystal momentum $\mathbf{k}$, and a denotes the Cartesian component. The real part of the dielectric function is then obtained from the calculated $\varepsilon''(\omega)$ by the Kramer-Kronig transformation [8,42]:

$$\varepsilon'(\omega) = 1 + \frac{2}{\pi} \mathbf{P} \int_0^\infty d\omega' \frac{\omega' \varepsilon''(\omega')}{\omega'^2 - \omega^2}. \quad (2)$$

Here $\mathbf{P}$ represents the principal value of the integral.

The imaginary part of the second-order optical susceptibility due to direct interband transitions is given by [8,9]

$$\chi_{abc}''^{(2)}(-2\omega, \omega, \omega) = \chi_{abc,\mathrm{VE}}''^{(2)}(-2\omega, \omega, \omega) + \chi_{abc,\mathrm{VH}}''^{(2)}(-2\omega, \omega, \omega), \quad (3)$$

where the contribution due to the so-called virtual-electron (VE) process is [8,9]

$$\chi_{abc,\mathrm{VE}}''^{(2)} = -\frac{\pi}{2\Omega} \sum_{i\in \mathrm{VB}} \sum_{j,l\in \mathrm{CB}} \sum_{\mathbf{k}} w_{\mathbf{k}} \left\{ \frac{\mathrm{Im}\left[p_{jl}^a \langle p_{li}^b p_{ij}^c \rangle\right]}{\epsilon_{li}^3 (\epsilon_{li} + \epsilon_{ji})} \delta(\epsilon_{li} - \omega) - \frac{\mathrm{Im}\left[p_{ij}^a \langle p_{jl}^b p_{li}^c \rangle\right]}{\epsilon_{li}^3 (2\epsilon_{li} - \epsilon_{ji})} \delta(\epsilon_{li} - \omega) + \frac{16\mathrm{Im}\left[p_{ij}^a \langle p_{jl}^b p_{li}^c \rangle\right]}{\epsilon_{ji}^3 (2\epsilon_{li}^3 - \epsilon_{ji}^3)} \delta(\epsilon_{ji} - 2\omega) \right\}, \quad (4)$$

and that due to the virtual-hole (VH) process is [8,9]

$$\chi_{abc,\mathrm{VH}}''^{(2)} = \frac{\pi}{2\Omega} \sum_{i,l\in \mathrm{VB}} \sum_{j\in \mathrm{CB}} \sum_{\mathbf{k}} w_{\mathbf{k}} \left\{ \frac{\mathrm{Im}\left[p_{li}^a \langle p_{ij}^b p_{jl}^c \rangle\right]}{\epsilon_{jl}^3 (\epsilon_{jl} + \epsilon_{ji})} \delta(\epsilon_{jl} - \omega) - \frac{\mathrm{Im}\left[p_{ij}^a \langle p_{jl}^b p_{li}^c \rangle\right]}{\epsilon_{jl}^3 (2\epsilon_{jl} - \epsilon_{ji})} \delta(\epsilon_{jl} - \omega) + \frac{16\mathrm{Im}\left[p_{ij}^a \langle p_{jl}^b p_{li}^c \rangle\right]}{\epsilon_{ji}^3 (2\epsilon_{jl} - \epsilon_{ji})} \delta(\epsilon_{ji} - 2\omega) \right\}. \quad (5)$$

TABLE II. Calculated (E_g^{GGA} and $E_g^{\mathrm{HSE\text{-}SOC}}$) and experimental band gaps (E_g^{exp}) as well as scissors operators ($\Delta E_g = E_g^{\mathrm{HSE\text{-}SOC}} - E_g^{\mathrm{GGA}}$) for selenium and tellurium. The values in brackets are from the HSE calculations without the SOC.

	E_g^{GGA} (eV)	$E_g^{\mathrm{HSE\text{-}SOC}}$ (eV)	E_g^{exp} (eV)	ΔE_g (eV)
Se	1.002	1.735 (1.759)	2.0[a]	0.733
Te	0.113	0.322 (0.546)	0.323[b]	0.209

[a]Experimental value from Ref. [30].
[b]Experimental value from Ref. [44].

Here $\epsilon_{ji} = \epsilon_{\mathbf{k}j}$-$\epsilon_{\mathbf{k}i}$ and $\langle p_{jl}^b p_{li}^c \rangle = \frac{1}{2}(p_{jl}^b p_{li}^c + p_{li}^b p_{jl}^c)$. The real part of the second-order optical susceptibility is then obtained from the calculated $\chi_{abc}^{\prime\prime(2)}$ by the Kramer-Kronig transformation [8,9]:

$$\chi^{\prime(2)}(-2\omega, \omega, \omega) = \frac{2}{\pi}\mathbf{P}\int_0^\infty d\omega' \frac{\omega' \chi^{\prime\prime(2)}(2\omega', \omega', \omega')}{\omega'^2 - \omega^2}. \quad (6)$$

The LEO coefficient $r_{abc}(\omega)$ is related to the second-order optical susceptibility $\chi_{abc}^{(2)}(-\omega, \omega, 0)$ [5]. In the zero frequency limit,

$$r_{abc}(0) = -\frac{2}{\varepsilon_a(0)\varepsilon_b(0)} \lim_{\omega\to 0} \chi_{abc}^{(2)}(-2\omega, \omega, \omega). \quad (7)$$

Furthermore, for the photon energy ω well below the band gap, $\chi_{abc}^{(2)}(-2\omega, \omega, \omega)$ and $n(\omega)$ are nearly constant. In this case, the LEO coefficient $r_{abc}(\omega) \approx r_{abc}(0)$ [8,10].

To obtain accurate optical properties, we perform calculations for selenium and tellurium with several different k-point meshes until the calculated optical properties converge to a few percent. As a result, dense k-point meshes of $40 \times 40 \times 36$ and $50 \times 50 \times 38$ are adopted for selenium and tellurium, respectively. Furthermore, about 27 bands per atom are included in the optical calculations to ensure that ε' and $\chi^{\prime(2)}$ obtained by the Kramer-Kronig transformation are reliable, as confirmed by further test calculations for selenium using different numbers of bands. The function δ in Eqs. (1), (4), and (5) are approximated by a Gaussian function with $\Gamma = 0.2$ eV.

It is well known that the band gap of a semiconductor is generally underestimated by the local density approximation (LDA) and GGA calculations (see, e.g., Table II) where many-body effects, especially quasiparticle self-energy correction, are not adequately taken into account. On the other hand, Eqs. (1), (4), and (5) indicate that correct band gaps would be important for obtaining accurate optical properties. Therefore, we further perform the band-structure calculations using the hybrid Heyd-Scuseria-Ernzerhof (HSE) functional [45], which is known to produce much improved band gaps for semiconductors. We then take the self-energy corrections into account by the so-called scissors correction (SC) [46], using the accurate band gaps from the HSE calculations. In the SC calculation, the conduction bands are uniformly upshifted so the band gap would match the HSE gap together with the renormalized transition matrix elements [46]. Indeed, such SC calculations were shown to give rise to the second-order nonlinear susceptibility at zero frequency for low-dimensional materials such as trigonal selenium [4] and graphenelike BN sheets that agree well with the experimental ones [10].

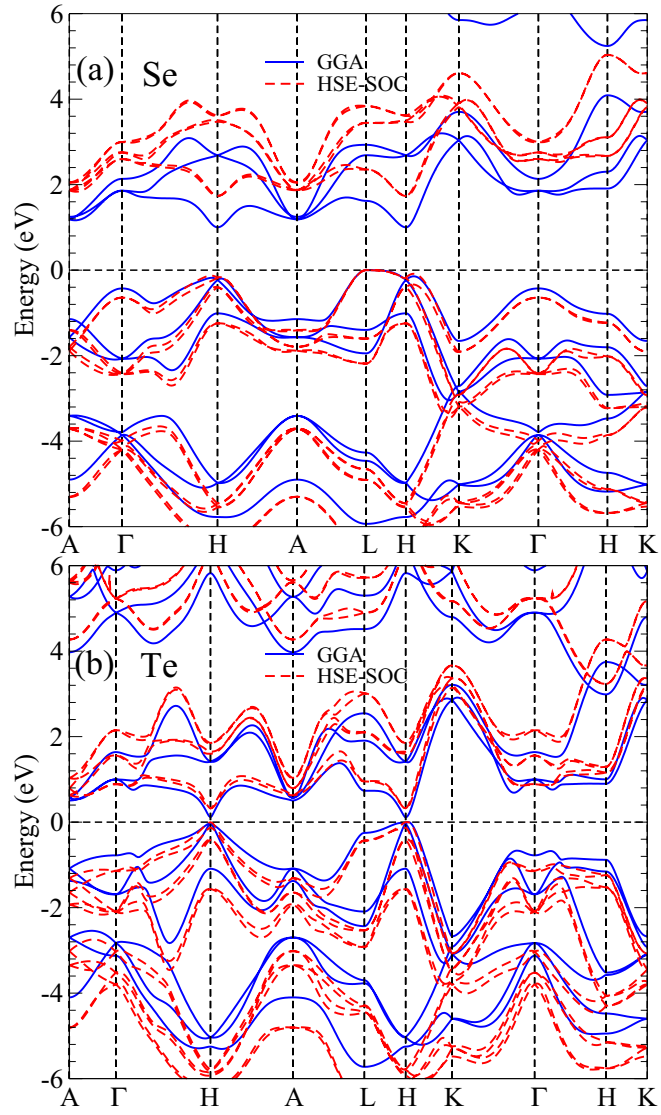

FIG. 2. Band structures of (a) selenium and (b) tellurium from the GGA (blue solid lines) calculations and HSE (red dashed lines) calculations with the SOC included. Both materials possess an indirect band gap. The top of the valence bands is at 0 eV.

III. RESULTS AND DISCUSSION

A. Electronic band structure

Because selenium and tellurium have the same crystalline structures, the band structure of selenium is similar to that of tellurium, as shown in Fig. 2. Both materials are indirect band-gap semiconductors which have the conduction band minimum (CBM) at the H point. For selenium, the valence band maximum (VBM) is located at the L point, whereas the VBM of tellurium is close to the H point along the H-K direction. The calculated band gap is 1.002 (0.113) eV in Se (Te), which is significantly smaller than the experimental value of 2.0 (0.323) eV [30,44]. The ratio between the interchain and intrachain distances of tellurium, as mentioned previously, is smaller than that of selenium. Thus, the enhanced interchain interaction in tellurium brings about more electrons transferred from lone pair states to antibonding states and this

weakens the Peierls distortion. This explains why the band gap of tellurium is smaller than that of selenium, even though they have the same crystalline structure. There are three groups of valence bands, namely, the *s* bonding, *p* bonding, and *p* lone pair states, and the three lowest conduction bands arise from the *p* antibonding states. The calculated band structures of Se and Te agree quite well with previous calculations [18]. The minor differences stem from the fact that the present GGA calculations are done without SOC.

As mentioned before, we also calculate the band structures by using the HSE functional [45] in order to get more accurate band gaps. The band structures from the HSE calculations with the SOC included are displayed in Fig. 2. The theoretical band gaps from the GGA and HSE calculations together with the experimental values are listed in Table II. Indeed, the band gaps of selenium and tellurium from the HSE calculations with the SOC included, are in good agreement with the corresponding experimental values (Table II). Therefore we use the band gap differences between the HSE-SOC calculations and GGA calculations as the scissors correction energy [46], to evaluate linear and NLO properties for both selenium and tellurium.

We also calculate total and orbital-projected DOS for selenium and tellurium, as displayed in Fig. 3. Overall, the DOS spectra of the two systems are rather similar. Hence, in what follows, we only analyze the DOS spectra of selenium. We can see from Fig. 3(a) that the lowest valence bands of selenium ranging from −15.9 to −9.5 eV (region VB1) stem mainly from the *s* orbitals. On the other hand, the top valence bands ranging from −5.9 to 0.0 eV (regions VB2 and VB3) and the lower conduction bands ranging from 1.0 to 4.0 eV (region CB1) originate primarily from the *p* orbitals. Figure 3(b) further shows that the lower valence bands ranging from −5.9 to −4.8 eV and also the conduction bands ranging from 1.9 to 4.0 eV are dominated by the p_z orbital with an equal contribution from the p_x and p_y orbitals. The top valence bands ranging from −4.8 to 0.0 eV are of mainly p_x and p_y orbitals with a certain p_z component. Moreover, the lower conduction bands ranging from 1.2 to 1.9 eV mainly consist of the p_x and p_y orbitals. Thus, Fig. 3 shows clearly that both the upper valence bands and lower conduction bands near the band gap are dominated by the *p* orbitals and hence the *p* orbitals will play a major role in the linear and NLO responses.

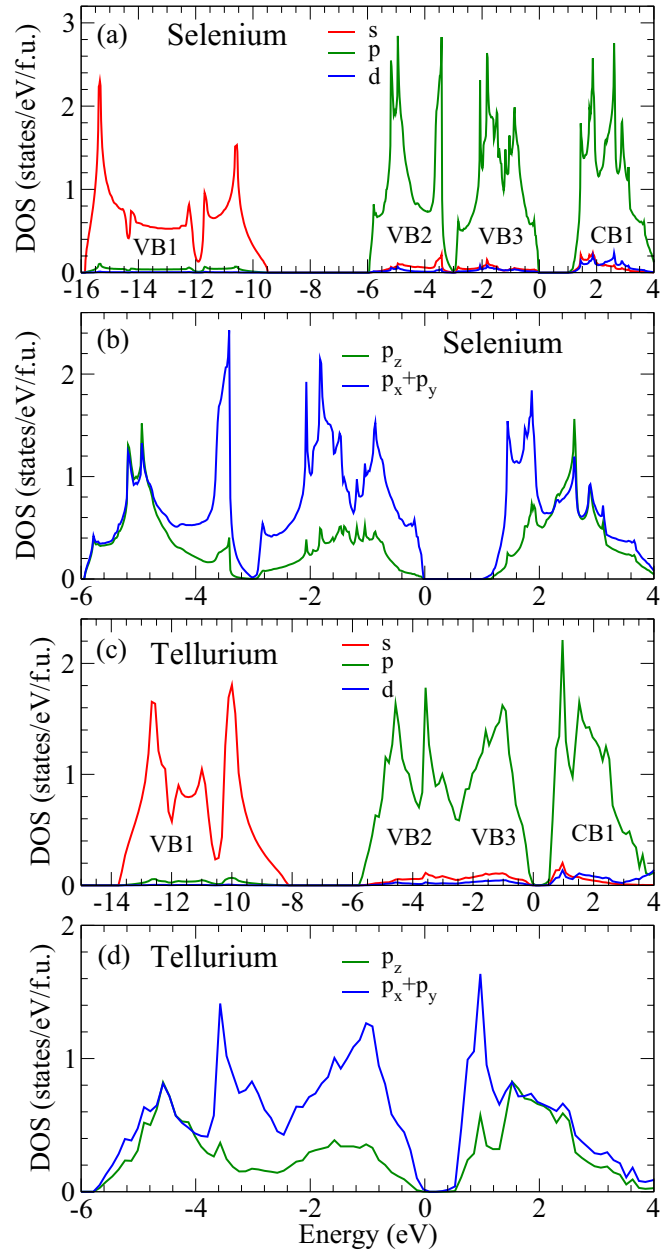

FIG. 3. Total and orbital-projected density of states (DOS) for selenium (a) and (b) as well as tellurium (c) and (d). The top of the valence bands is at 0 eV.

B. Linear optical property

The calculated imaginary (absorptive) part of the optical dielectric function $\varepsilon(\omega)$ for selenium and tellurium are shown in Fig. 4. Selenium and tellurium have a uniaxial crystalline structure with strongly covalent bonded spiral chains oriented along the *c* axis which are weakly binded by van der Waals forces. As a result, their optical properties depend significantly on light polarization direction. Thus, the imaginary part of the dielectric function for both systems consist of two distinctly different components, i.e., light polarization parallel ($E \parallel c$) and perpendicular ($E \parallel a$) to the *c* axis. In particular, Fig. 4(a) shows that the absorptive part of $E \parallel a$ is much smaller than that of $E \parallel c$ in the low energy range (about 2.3 ∼ 8.8 eV), while it is the opposite in the energy range above 8.8 eV. Although the similar phenomena are observed in tellurium, it possesses weaker optical anisotropy than selenium (Fig. 4). This could be explained by the fact that tellurium has a weaker structural anisotropy.

Figure 4(a) shows that there are two pronounced peaks in the imaginary part of the dielectric function for $E \parallel c$, namely, a large peak (C_2) located at ∼3.7 eV and a relatively small one (C_4) in the neighborhood of 7.5 eV. Furthermore, there are three shoulder peaks at ∼2.4 eV (C_1), ∼6.1 eV (C_3), and ∼8.7 eV (C_5), respectively. For $E \parallel a$, our theoretical calculations for selenium exhibit a prominent peak (A_2) near 3.7 eV. Beyond that, for $E \parallel a$, the spectrum shows multiple bumps ($A_3 \sim A_8$). The amplitude of the bumps above ∼5.6 eV

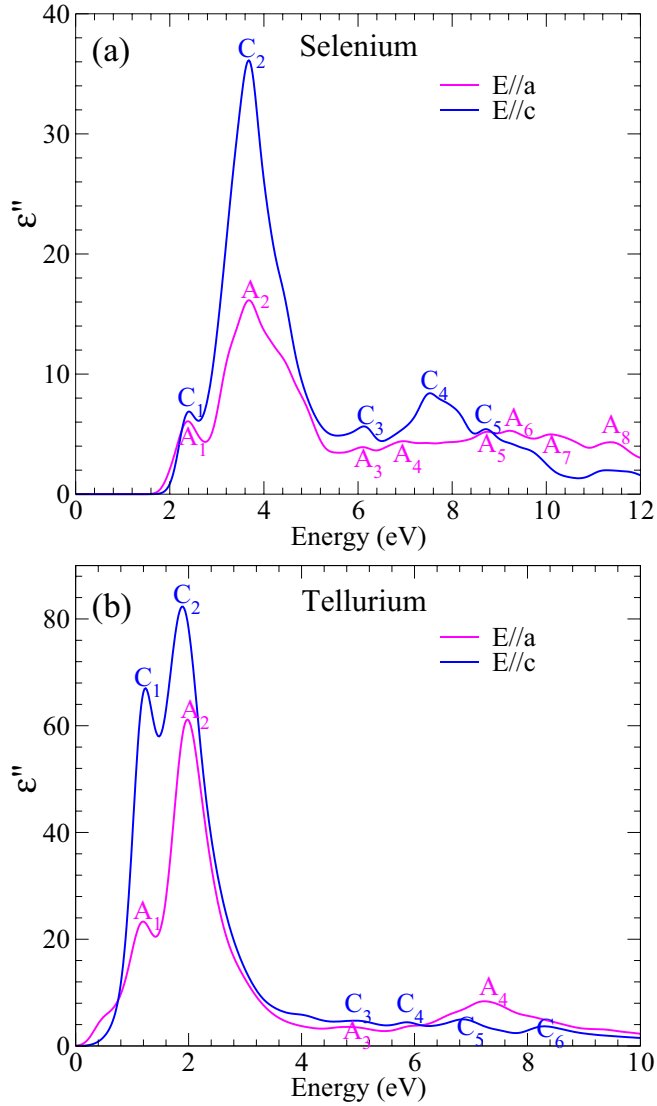

FIG. 4. The absorptive part of optical dielectric function $\varepsilon''(\omega)$ of (a) selenium and (b) tellurium for both light polarization perpendicular (E ∥ a) and parallel (E ∥ c) to the c axis.

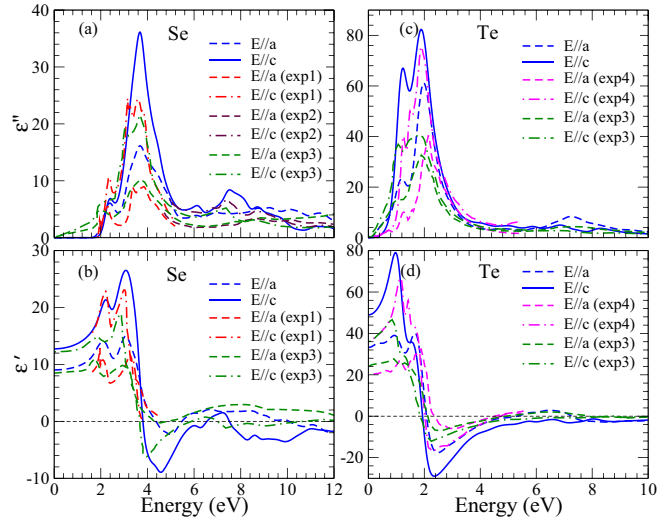

FIG. 5. Calculated and experimental imaginary $[\varepsilon''(\omega)]$ and real part $[\varepsilon'(\omega)]$ of the dielectric function for (a) and (b) selenium as well as (c) and (d) tellurium for both light polarization perpendicular (E ∥ a) and parallel (E ∥ c) to the c axis. Red, maroon, green, and magenta dashed and dot-dashed lines denote the measured dielectric function spectra from Refs. [30] (exp1), [48] (exp2), [49] (exp3), and [50] (exp4), respectively.

increases and then decreases with the photon energy. At 5.6 eV occurs a deep minimum deriving from the fact that transitions from the upper valence triplet to the lower conduction triplet are already exhausted. The amplitude of the bumps increases within the energy range between 5.6 eV and 9.2 eV due to the transitions from the lower valence triplet to the lower conduction triplet and also from the upper valence triplet to the upper conduction triplet. For Te, Fig. 4(b) shows that the spectra of the imaginary part of the dielectric function could be divided into two regions. In the low-energy region (about 0–4 eV), there are two prominent peaks for both $E \parallel a$ (A_1, A_2) and $E \parallel c$ (C_1, C_2). The larger peak (A_2) occurs at ∼2.0 eV and the smaller peak (A_1) is found at 1.2 eV for $E \parallel a$. For $E \parallel c$, the larger (C_2) and smaller (C_1) peaks are located at 1.9 eV and ∼1.2 eV, respectively. In the high-energy region (about 4–9 eV), a broad peak (A_4) centered at ∼7.2 eV for $E \parallel a$ exists. However, the spectrum of $E \parallel c$ exhibits some steadily oscillatory bulges in the energy region. Therefore, the transitions from the lower valence triplet to the lower conduction triplet and from the upper valence triplet to the upper conduction triplet are more pronounced.

The calculated and experimental [47] static dielectric constants are listed in Table VII. It is clear from Table VII that the dielectric constants of both selenium and tellurium from the GGA calculations with the scissors correction agree well with the measured ones while, as expected, that obtained from the GGA calculations without the scissors correction are too large. The measured optical dielectric functions for selenium and tellurium [48,49] are compared with our calculations in Fig. 5. The imaginary part of the dielectric function would allow us to find out the information on the major electronic transitions. Thus, we focus on the calculated and experimental spectra of the imaginary part of the dielectric function. First, we find that for selenium, the positions of the A_2 and C_2 peaks at ∼3.7 eV are consistent with the experiments [49]. Furthermore, small bumps C_3 and C_5 are also observed in the experimental spectra [48]. In particular, the position of the C_5 bump is consistent with the experiment [48]. Moreover, Fig. 5(a) shows that our calculated five small bumps (A_3, A_4, A_5, A_7, A_8) agree reasonably well with that of the measurements [48], other than having slightly larger amplitudes. The experiment and our theoretical calculations have common peaks A_1, C_1, and C_4, although the energy positions of the theoretical peaks are slightly blueshifted compared to that of the experimental ones [48,49]. Finally, the positions of peaks A_1 and C_1 are consistent with the experiments [30].

For tellurium, the positions of peaks A_1, A_2, A_3, A_4, C_1, and C_2 in the imaginary part of the dielectric function agree well with that of the experimental spectra [49,50]. Furthermore, the small C_3, C_5, and C_6 peaks can also be observed in the experimental [49] spectra, other than being redshifted by

TABLE III. Symmetry adapted basis functions of the point groups for six high-symmetry k-points in the hexagonal Brillouin zone [see Fig. 1(c)].

Group	k-point	A_1	A_2	E	A	B
D_3	A, Γ, H, K	s, d_{z^2}	p_z	$p_x, p_y,$ $d_{xz}, d_{yz},$ $d_{xy}, d_{x^2-y^2}$		
C_2	L, M				$p_z, d_{xy},$ $d_{z^2}, d_{x^2-y^2}$	$p_x, p_y,$ d_{xz}, d_{yz}

about 0.2 eV, 0.2 eV, and 0.4 eV, respectively. In the high energy region (4.0–9.0 eV), both the calculated and experimental [49] spectra exhibit oscillatory peaks, although the positions of the peaks differ slightly. Overall, the theoretical imaginary part of the dielectric function for both materials are in good agreement with the experiments. Furthermore, Figs. 5(b) and 5(d) show that the spectral shape of the real part of the dielectric function agrees rather well with that of the experiments [49,50].

The band structure and linear optical properties of selenium and tellurium have been studied both theoretically [33,48,51,52] and experimentally [30,31,44,48,49] before. Nevertheless, no detailed analysis on the main peaks in the imaginary part of the dielectric function in terms of interband transitions, has been reported. Here we perform such a detailed analysis. Equations (1), (4), and (5) show that the imaginary parts of the dielectric function and second-order NLO susceptibility are closely connected with the dipole-allowed interband transitions. Thus, we can understand the origin of the peaks in the imaginary part of the dielectric function by analyzing the symmetry of the band states and also the dipole transition selection rules. First, by using the projection method of the group theory, we deduce the symmetry-adapted basis functions in terms of the atomic orbitals (Table III). Second, we determine the symmetry of the band states (Fig. 6) for six principal symmetry points (A, Γ, H, L, K, M) by comparing the symmetry-adapted basis functions with the calculated orbital characters of the band states at the six symmetry points. Note that the atomic configurations of Se and Te are $4s^2$, $4p^4$ and $5s^2$, $5p^4$. Therefore, we only consider the symmetry-adapted basis functions of s, p_x, p_y, and p_z orbitals. Such deduced symmetries at the $A, \Gamma, H,$ and K points are consistent with the previous calculations [51]. After considering the selection rules (Table IV) [52], we could assign the peaks in the imaginary part of the dielectric function to the direct interband transitions at the six symmetry points, as shown in Fig. 6 as well as in Tables V and VI. For example, for trigonal

TABLE IV. Dipole selection rules between the band states at six high symmetry k-points in the hexagonal Brillouin zone [see Fig. 1(c)].

	$E \perp c$	$E \parallel c$		$E \perp c$	$E \parallel c$
D_3	$\Gamma_1 \longleftrightarrow \Gamma_3$	$\Gamma_1 \longleftrightarrow \Gamma_2$	C_2	$\Gamma_1 \longleftrightarrow \Gamma_2$	$\Gamma_1 \longleftrightarrow \Gamma_1$
Γ	$\Gamma_2 \longleftrightarrow \Gamma_3$	$\Gamma_3 \longleftrightarrow \Gamma_3$	L	$\Gamma_1 \longleftrightarrow \Gamma_3$	$\Gamma_2 \longleftrightarrow \Gamma_2$
(A, H, K)	$\Gamma_3 \longleftrightarrow \Gamma_3$		(M)	$\Gamma_2 \longleftrightarrow \Gamma_3$	$\Gamma_3 \longleftrightarrow \Gamma_3$

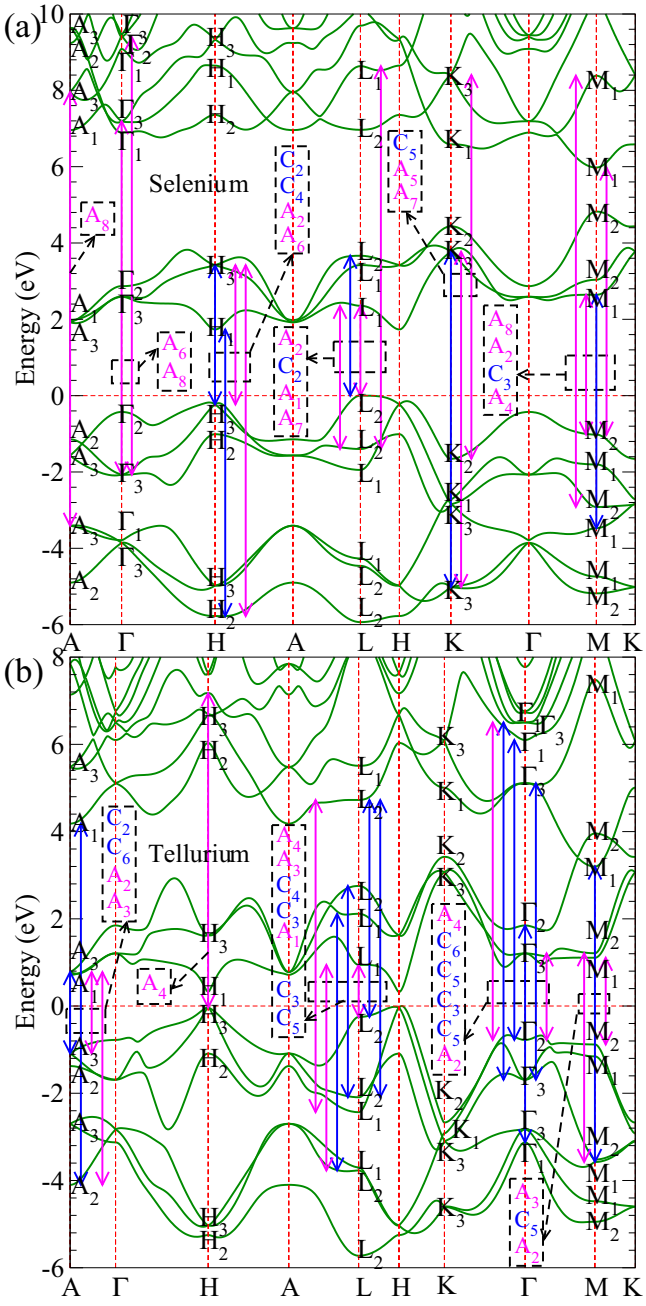

FIG. 6. (a) Selenium and (b) tellurium band structures from the GGA calculation with the scissors correction. The symmetries of band states at six high-symmetry points are labeled according to the irreducible representations of the point groups (Table III). The principal interband transitions and the peaks in the imaginary part of the dielectric function in Fig. 4 are indicated by blue [light polarized parallel (E ∥ c) to the c axis] and pink [light polarized perpendicular (E ∥ a) to the c axis] arrows. The top of the valence bands is at 0 eV.

selenium, the A_2 peak at ∼3.7 eV [see Fig. 4(a)] stems from transitions from the H_3 state at the top of the valence band to the conduction band state H_3 (∼3.4 eV) at H-point and from the L_2 valence band state at −1.4 eV to the L_1 state at the bottom of conduction band at the L-point. Furthermore, the A_2 peak is associated with the transition from the M_2 state at the top of valence band to the M_1 state at the bottom of

TABLE V. The principal peaks in the imaginary part spectra of the dielectric function [see Fig. 4(a)] and corresponding direct interband transitions at six high symmetry k-points [see Fig. 6(a)] for selenium.

Peak	Direct transitions	Peak	Direct transitions
C_1		A_1	$L:9\rightarrow 10$
C_2	$H:8,9\rightarrow 11,12$; $L:9\rightarrow 12$	A_2	$H:8,9\rightarrow 11,12$; $L:8\rightarrow 10$; $M:9\rightarrow 10$
C_3	$M:6\rightarrow 10$	A_3	
C_4	$H:4\rightarrow 10$	A_4	$M:9\rightarrow 13$
C_5	$K:4,5\rightarrow 10,11$	A_5	$K:4,5\rightarrow 10,11$
		A_6	$\Gamma:7,8\rightarrow 14,15$; $H:4\rightarrow 11,12$
		A_7	$K:9\rightarrow 14,15$; $L:8\rightarrow 14$
		A_8	$A:3\rightarrow 10,11$; $A:5,6\rightarrow 14,15$; $\Gamma:7,8\rightarrow 17$; $M:7\rightarrow 14$

conduction band at M-point. The C_2 peak at ∼3.7 eV could be attributed to transitions starting from the H_3 state at the top of valence band to the conduction band states H_3 (∼3.4 eV) at the H-point and from the L_2 state at the top of valence band to the L_2 conduction band state (∼3.7 eV) at the L-point.

Similarly, for tellurium, we can assign the A_2 peak [see Fig. 4(b)] to the transitions from the Γ_2 state at the top of valence band to the Γ_3 state at the bottom of conduction band at the Γ-point and from the M_2 state at the top of valence band to the M_1 state at the bottom of conduction band at the M-point. It is noted that the transition from the A_3 state at the top of the valence band to the conduction band state A_3 (∼0.8 eV) at the A-point contributes to the A_2 and C_2 peaks.

TABLE VI. The principal peaks in the imaginary part spectra of the dielectric function [see Fig. 4(b)] and corresponding direct interband transitions at six high-symmetry k-points [see Fig. 6(b)] for tellurium.

Peak	Direct transitions	Peak	Direct transitions
C_1		A_1	$L:9\rightarrow 10$
C_2	$A:8,9\rightarrow 11,12$	A_2	$A:8,9\rightarrow 11,12$; $\Gamma:9\rightarrow 10,11$; $M:9\rightarrow 10$
C_3	$\Gamma:4\rightarrow 12$; $L:8\rightarrow 12$; $L:9\rightarrow 13$	A_3	$A:4\rightarrow 11,12$; $L:5\rightarrow 10$; $M:6\rightarrow 11$
C_4	$L:6\rightarrow 11$	A_4	$\Gamma:9\rightarrow 16,17$; $H:8,9\rightarrow 16$; $L:7\rightarrow 13$
C_5	$\Gamma:7,8\rightarrow 13,14$; $\Gamma:9\rightarrow 15$; $M:6\rightarrow 12$; $L:8\rightarrow 13$		
C_6	$A:4\rightarrow 13$; $\Gamma:7,8\rightarrow 16,17$		

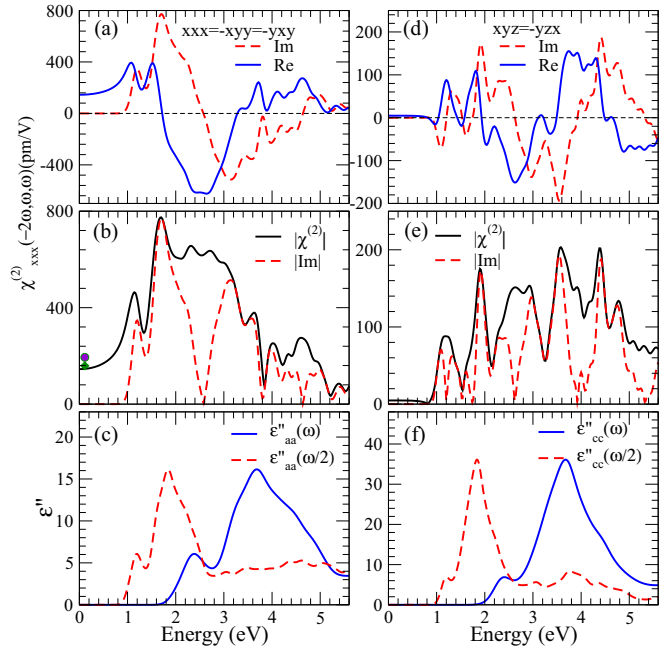

FIG. 7. (a) and (d) Real and imaginary parts as well as (b) and (e) absolute value of the second-order susceptibility (a) and (b) $\chi^{(2)}_{xxx}$ as well as (d) and (e) $\chi^{(2)}_{xyz}$ of selenium. (c) and (f) Imaginary part $\varepsilon''(\omega)$ of the dielectric function for light polarization perpendicular and parallel to the c axis, respectively. In (b), the green diamond and violet circle denote the experimental SHG values from Refs. [29] and [32], respectively.

C. Second-harmonic generation and linear electro-optic coefficient

Point group D_3 has ten nonvanishing second-order NLO susceptibility elements [1,2]. However, the crystalline symmetry D_3^4 of selenium and tellurium further reduces this number to five. Our *ab initio* calculations show that there are only two independent elements among the five nonzero elements because $\chi^{(2)}_{xxx}=-\chi^{(2)}_{xyy}=-\chi^{(2)}_{yxy}$, $\chi^{(2)}_{xyz}=-\chi^{(2)}_{yzx}$. Our calculations for selenium also reveal that the values of the $\chi^{(2)}_{xxx}$ element of the two helical structures (D_3^4 and D_3^6) are equal but the values of the $\chi^{(2)}_{xyz}$ element differ in sign. Therefore, here we present only $\chi^{(2)}_{xxx}$ and $\chi^{(2)}_{xyz}$ for space group D_3^4, as mentioned above in Sec. II. The calculated real and imaginary parts as well as the absolutes values of these two elements are displayed in Figs. 7 and 8 for selenium and tellurium, respectively. We note that with the scissors correction, the line shapes of the calculated NLO spectra are hardly changed and thus only the NLO spectra calculated with the scissors correction are displayed in Figs. 7 and 8. However, the peak positions are blueshifted by about the energy of the scissors correction (ΔE_g). Moreover, the magnitude of the second-order susceptibility gets reduced (see Table VII).

In Table VII, we list the calculated static dielectric constant $\varepsilon(0)$, second-order NLO susceptibility $\chi^{(2)}(0,0,0)$, and zero-frequency LEO coefficient $r(0)$. Interestingly, Table VII shows that tellurium exhibits large static second-order NLO susceptibility, especially $\chi^{(2)}_{xyz}(0)$, which is up to 100 times larger than that of GaN in both zinc-blende and wurtzite

TABLE VII. Static dielectric constants ($\varepsilon_x = \varepsilon_y$ and ε_z), second-order susceptibility $\chi^{(2)}_{xxx}(0)$ (pm/V), $\chi^{(2)}_{xyz}(0)$ (pm/V), and $|\chi^{(2)}_{xxx}(0.113\,\text{eV})|$ (pm/V) as well as LEO coefficient $r_{xxx}(0)$ (pm/V) and $r_{xyz}(0)$ (pm/V) of selenium and tellurium calculated without (GGA) and with (SC) scissors correction. Available experimental data and previous calculation are also listed for comparison.

		ε_x	ε_z	$\chi^{(2)}_{xxx}(0)$	$\chi^{(2)}_{xyz}(0)$	$r_{xxx}(0)$	$r_{xyz}(0)$	$\lvert\chi^{(2)}_{xxx}(0.113\,\text{eV})\rvert$
Se	GGA	10.8	15.4	330, 440[a]	6	−5.63	−0.10	335
	SC	9.0	12.7	145, 194[b]	5	−3.58	−0.12	146
	exp	6.2∼8.4[b]	12.7[b]					159 ± 84[c]
								194 ± 50[d]
Te	GGA	40.6	57.2					3163
	SC	33.2	49.0	169	1009	−0.30	−1.82	475
	exp	33.0[b]	54.0[b]					1840 ± 560[d]
								1843 ± 586[e]

[a]LDA calculations with the SC from Ref. [4].
[b]Experimental value from Ref. [47].
[c]Experimental value from Ref. [29].
[d]Experimental value from Ref. [32].
[e]Experimental value from Ref. [33].

structures [6,7]. Furthermore, for both materials, the static second-order NLO susceptibility exhibits strong anisotropy. The same phenomenon is observed in the LEO coefficient. Moreover, selenium has large LEO coefficient $r_{xxx}(0)$ (∼3.6 pm/V), being more than six times larger than that of bulk GaN polytypes [6,7].

Let us now compare our calculated $|\chi^{(2)}_{xxx}(0)|$ and $|\chi^{(2)}_{xxx}(0.113)|$ with the previous LDA calculations and available experiments. First, our calculated $|\chi^{(2)}_{xxx}(0.113)|$ for selenium agrees rather well with the experimental values reported in Ref. [29] and also Ref. [32] [see Table VII and Fig. 7(b)]. Second, for $|\chi^{(2)}_{xxx}(0)|$, the agreement between our GGA calculations and the previous LDA calculations [4] is also rather good (see Table VII). For tellurium, Table VII and Fig. 8(b) show that our calculated $|\chi^{(2)}_{xxx}(0.113)|$ is much smaller than the available experiment values [32,33]. Nonetheless, we note that in the energy range of 0.0 ∼ 0.3 eV, $|\chi^{(2)}_{xxx}|$ increases rapidly with the photon energy and the energy of 0.113 eV sits right at the middle of the steep slope [Fig. 8(b)]. Thus, a small error in the energy position could cause a large discrepancy between the theory and experiment. Indeed a small redshift (∼0.1 eV) could bring the calculated and experimental values of $|\chi^{(2)}_{xxx}(0.113)|$ in good agreement.

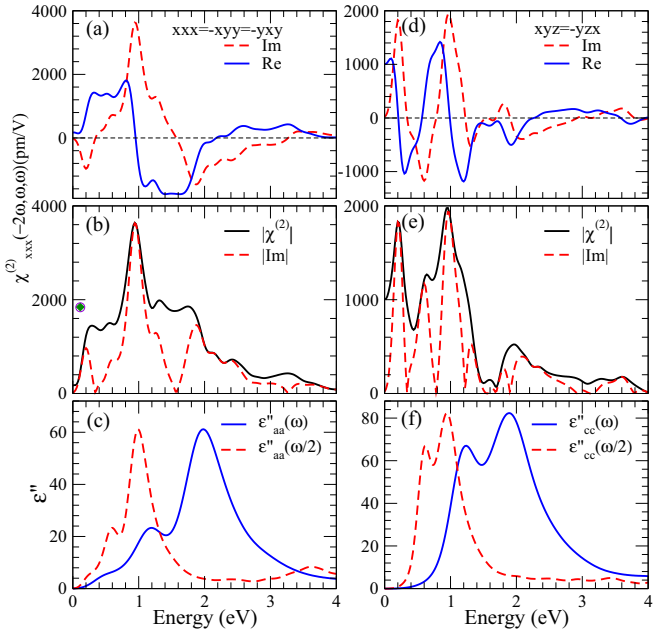

FIG. 8. (a) and (d) Real and imaginary parts as well as (b) and (e) absolute value of the second-order susceptibility (a) and (b) $\chi^{(2)}_{xxx}$ as well as (d) and (e) $\chi^{(2)}_{xyz}$ of tellurium. (c) and (f) Imaginary part $\varepsilon''(\omega)$ of the dielectric function for light polarization perpendicular and parallel to the c axis, respectively. In (b), the green diamond and violet circle denote the experimental SHG values from Refs. [32] and [33], respectively.

The SHG involves not only single-photon (ω) resonance but also double-photon (2ω) resonance. Therefore, to further analyze the NLO responses, we plot the modulus of the imaginary parts of the second-order susceptibility $|\chi^{(2)}(-2\omega,\omega,\omega)|$ as well as dielectric functions $\varepsilon''(\omega)$ and $\varepsilon''(\omega/2)$ together in Figs. 7 and 8 for selenium and tellurium, respectively, to understand the prominent features in the spectra of $\chi^{(2)}(-2\omega,\omega,\omega)$. For selenium, Fig. 7 shows that the threshold of the $\chi^{(2)}(-2\omega,\omega,\omega)$ spectra and also the absorption edge of $\varepsilon''(\omega/2)$ is at ∼0.87 eV ($\frac{1}{2}E_g$), while the absorption edge of $\varepsilon''(\omega)$ is at ∼1.73 eV (E_g). Therefore, the SHG spectra can be divided into two parts. The first part from 0.87 to 2.50 eV stems predominantly from double-photon resonances. The second part (above 2.5 eV) is mainly associated single-photon resonances with some contribution from double-photon resonances [see Figs. 7(c) and 7(f)]. These two types of resonances cause the SHG spectra to oscillate and decrease gradually in the higher energy region. Figure 7 indicates that, for selenium, both the real and imaginary parts of the second-order NLO susceptibility $\chi^{(2)}_{xyz}(-2\omega,\omega,\omega)$ show an oscillatory behavior with the energy. Indeed, the spectrum of $|\chi^{(2)}_{xyz}(-2\omega,\omega,\omega)|$ oscillates rapidly and has the maximum of about 205 pm/V at ∼3.6 eV [see Fig. 7(e)]. It is clear from Fig. 7(b) that the spectrum of the absolute value of $\chi^{(2)}_{xxx}(-2\omega,\omega,\omega)$ shows a broad plateau from 1.34 eV to 3.44 eV and reaches the maximum of 775 pm/V at 1.7 eV which is a few times larger than that of GaN [6,7], a widely used NLO semiconductor.

For tellurium, likewise, the spectral structure in the energy range from ∼0.16 ($\frac{1}{2}E_g$) to ∼1.0 eV is formed mainly by double-photon (2ω) resonances. The rest structure (above ∼1.0 eV) arises mainly from single-photon (ω) resonances with some contribution from 2ω resonances. All the NLO susceptibilities of tellurium are large in the photon energy range of 0.0 ∼ 3.0 eV. For example, the magnitude of $|\chi^{(2)}_{xyz}(-2\omega,\omega,\omega)|$ is around 1977 pm/V at 0.96 eV. Interestingly, for both systems, the real part, imaginary part, and absolute value of $\chi^{(2)}_{xyz}$ are smaller than $\chi^{(2)}_{xxx}$, and produce relatively pronounced oscillations compared to $\chi^{(2)}_{xxx}$. The phenomenon is explained by the fact that the two materials are helical chains along the c axis and possess a high degree of anisotropy. In particular, the absolute value of second-order NLO susceptibility $\chi^{(2)}_{xxx}$ of tellurium is as high as 3640 pm/V at 0.94 eV, which is nearly 16 times larger than that of GaN [6,7]. This suggests that tellurium would be a superior NLO material and has potential application in NLO and LEO optical devices such as frequency conversion, optical switching, SHG, optical modulation, and sensing devices.

Equations (1), (4), and (5) show that for a specific semiconductor, the smaller the band gap is, the larger the magnitude of the imaginary part of the dielectric function, and second-order NLO susceptibility would be, simply because of the energy differences between the initial and final states of optical excitations in the denominators. In particular, the magnitude of the imaginary part of the SHG coefficients especially in the low-frequency region would be roughly proportional to the inverse of the fourth power of the band gap. Table II shows that tellurium has a band gap which is roughly six times smaller than that of selenium, and this explains why the calculated $\chi^{(2)}$ values of tellurium are much larger than that of selenium (see Table VII and Figs. 7 and 8), although the two materials have similar crystalline and electronic structures. However, if the band gap is too small, especially when the band gap is smaller than the optical frequencies of interest, the material would not be useful for the NLO applications because of the strong absorptions by the material. This suggests that to search for NLO materials with large SHG coefficients, one could focus on those semiconductors with smallest possible band gaps which are larger than the optical frequencies required by specific NLO applications.

To further investigate the origins of the enhanced NLO responses of selenium and tellurium, we also calculate the deformation charge density which is defined as the difference between the valence charge density and the superposition of the free atomic charge densities, as displayed in Fig. 9. Figure 9 clearly show that there is a considerable electron charge buildup in the vicinity of the Se-Se (Te-Te) bond center by depleting the charge around the atoms along the bond directions, resulting in strong directional covalent bonding. This strong covalency which would lead to large optical matrix elements due to large spatial overlap between the wave functions of initial and final states, and high anisotropy which would result in large joint DOS, would give rise to large $\chi^{(2)}$ values [53,54]. Moreover, Fig. 9 also shows a charge buildup around each atom in the direction perpendicular to the chain, indicating the existence of lone-pair electrons. The presence of lone-pair electrons is beneficial to the generation of induced dipole oscillations by the optical electric fields, thus leading

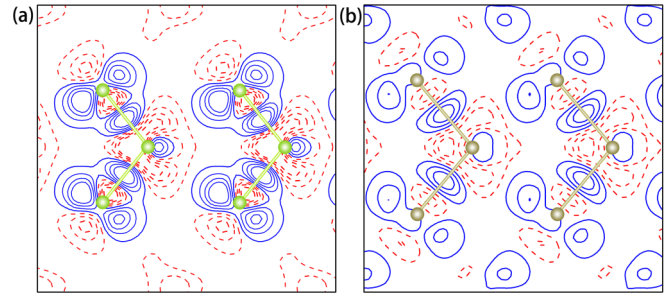

FIG. 9. The contour plots of the deformation charge densities for (a) selenium and (b) tellurium. The contour interval is 0.02 e/Å^3. The electron accumulation is depicted by positive contours (blue solid lines), while the electron depletion is represented by negative contours (red dashed lines).

to large SHG effects [55,56]. Therefore, in general, quasi-one-dimensional crystals with strong directional covalency and lone-pair electrons would have large $\chi^{(2)}$ values. This explains that selenium has much larger SHG coefficients than the semiconductors with similar band gaps such as GaAs [54]. This also suggests another strategy for designing good NLO materials with a specified band gap, namely, starting with chainlike semiconductors with strong covalency and/or lone-pair electrons.

IV. CONCLUSION

Summarizing, we have calculated the linear and NLO properties of trigonal selenium and tellurium based on the DFT with the GGA. To adequately take into account many-body effects, especially quasiparticle self-energy correction, we further perform the relativistic band-structure calculations using the hybrid HSE functional and use the much-improved band gaps to calculate the optical properties with the scissors correction. We find that the two materials exhibit large SHG and LEO effects. Also, their linear and NLO responses are highly anisotropic due to their structural anisotropy. In particular, the second-order NLO susceptibilities of tellurium are huge in the photon energy range of 0 ∼ 3 eV, with the magnitudes of $\chi^{(2)}_{xxx}$ being as large as 3640 pm/V, which is about 16 times larger than that of GaN, a widely used NLO material. Furthermore, tellurium is found to exhibit gigantic static SHG coefficients with the $\chi^{(2)}_{xyz}$ component being up to 100 times larger than that of GaN. On the other hand, selenium is shown to possess large LEO coefficient $r_{xxx}(0)$ which is more than six times larger than that of GaN polytypes. Thus, tellurium and selenium are excellent NLO materials and may find valuable applications in NLO and LEO devices such as electro-optical switches, frequency conversion, phase matching, and light signal modulators. Interestingly, our calculations also reveal that for the two different helical structures of each material, the values of $\chi^{(2)}_{xxx}$ are equal but the values of $\chi^{(2)}_{xyz}$ differ in sign, thus suggesting that the SHG spectroscopy is a useful probe of the chirality of these helical materials. The calculated static dielectric constants and also SHG coefficients at the CO_2 laser frequency are in good agreement with the experiments. Moreover, the energy positions and shapes of the principal features in the calculated optical dielectric function spectra of both

materials agree rather well with the available experimental ones. They are also analyzed in terms of the calculated electronic band structures, especially symmetries of the involved band states and dipole transition selection rules. The prominent structures in the spectra of $\chi^{(2)}(-2\omega, \omega, \omega)$ are also related to single-photon and double-photon resonances. Finally, much larger NLO coefficients in selenium and tellurium compared with the semiconductors with similar band gaps are attributed to their quasi-one-dimensional structures with directional covalent bonding and lone-pair electrons. We believe that our work will stimulate further experiments on the NLO and LEO effects in these interesting materials.

ACKNOWLEDGMENTS

M.C. thanks the Department of Physics and Center for Theoretical Physics, National Taiwan University for its hospitality during her three months visit there when parts of this work were carried out. Work at Xiamen University is supported by the National Key R&D Program of China (Grant No. 2016YFA0202601) and the National Natural Science Foundation of China (Grant No. 11574257). G.Y.G. acknowledges support from the Ministry of Science and Technology, the Academia Sinica Thematic Research Program (Grant No. AS-TP-106-M07), and the National Center for Theoretical Sciences in Taiwan.

[1] Y. R. Shen, *The Principle of Nonlinear Optics* (John Wiley and Sons Inc., New Jersey, 2003).

[2] R. W. Boyd, *Nonlinear Optics* (Elsevier Science, Amsterdam, 2003).

[3] R. K. Chang, J. Ducuing and N. Bloembergen, Dispersion of the Optical Nonlinearity in Semiconductoros, Phys. Rev. Lett. **15**, 415 (1965).

[4] H. Zhong, Z. H. Levine, D. C. Allan, and J. W. Wilkins, Band-theoretical calculation of the optical activity tensor of α-quartz and trigonal Se, Phys. Rev. B **48**, 1384 (1993).

[5] J. L. P. Hughes and J. E. Sipe, Calculation of second-order optical response in semiconductors, Phys. Rev. B **53**, 10751 (1996).

[6] V. I. Gavrilenko and R. Q. Wu, Linear and nonlinear optical properties of group-III nitrides, Phys. Rev. B **61**, 2632 (2000).

[7] D. Cai and G.-Y. Guo, Tuning linear and nonlinear optical properties of wurtzite GaN by *c*-axial stress, J. Phys. D: Appl. Phys. **42**, 185107 (2009).

[8] G. Y. Guo, K. C. Chu, D.-S. Wang, and C.-G. Duan, Linear and nonlinear optical properties of carbon nanotubes from first-principles calculations, Phys. Rev. B **69**, 205416 (2004).

[9] G. Y. Guo and J. C. Lin, Second-harmonic generation and linear electro-optical coefficients of BN nanotubes, Phys. Rev. B **72**, 075416 (2005); Erratum: Second-harmonic generation and linear electro-optical coefficients of BN nanotubes [Phys. Rev. B **72**, 075416 (2005)], **77**, 049901 (2008).

[10] C.-Y. Wang and G.-Y. Guo, Nonlinear optical properties of transition-metal dichalcogenide MX_2 (M= Mo, W; X= S, Se) monolayers and trilayers from first-principles calculations, J. Phys. Chem. C **119**, 13268 (2015).

[11] L. Hu, X. Huang, and D. Wei, Layer-independent and layer-dependent nonlinear optical properties of two-dimensional GaX (X= S, Se, Te) nanosheets, Phys. Chem. Chem. Phys. **19**, 11131 (2017).

[12] H. Wang and X. Qian, Giant optical second harmonic generation in two-dimensional multiferroics, Nano Lett. **17**, 5027 (2017).

[13] S. R. Panday and B. M. Fregoso, Strong second harmonic generation in two-dimensional ferroelectric IV-monochalcogenides, J. Phys.: Condens. Matter **29**, 43LT01 (2017); Corrigendum: Strong second harmonic generation in two-dimensional ferroelectric IV-monochalcogenides (2017 J. Phys.: Condens. Matter 29 43LT01), **30**, 179501 (2018).

[14] Q. Wu and X.-C. Zhang, Ultrafast electro-optic field sensors, Appl. Phys. Lett. **68**, 1604 (1996).

[15] P. Krusius, J. von Boehm, and T. Stubb, The self-consistent electronic structure of trigonal selenium, Phys. Status Solidi B **67**, 551 (1975).

[16] L. A. Agapito, N. Kioussis, W. A. Goddard III, and N. P. Ong, Novel Family of Chiral-Based Topological Insulators: Elemental Tellurium Under Strain, Phys. Rev. Lett. **110**, 176401 (2013).

[17] H. Peng, N. Kioussis, and G. J. Snyder, Elemental tellurium as a chiral *p*-type thermoelectric material, Phys. Rev. B **89**, 195206 (2014).

[18] M. Hirayama, R. Okugawa, S. Ishibashi, S. Murakami, and T. Miyake, Weyl Node and Spin Texture in Trigonal Tellurium and Selenium, Phys. Rev. Lett. **114**, 206401 (2015).

[19] K. Nakayama, M. Kuno, K. Yamauchi, S. Souma, K. Sugawara, T. Oguchi, T. Sato, and T. Takahashi, Band splitting and Weyl nodes in trigonal tellurium studied by angle-resolved photoemission spectroscopy and density functional theory, Phys. Rev. B **95**, 125204 (2017).

[20] T. W. Smith and R. A. Cheatham, Functional polymers in the generation of colloidal dispersions of amorphous selenium, Macromolecules **13**, 1203 (1980).

[21] D. R. Mees, W. Pysto, and P. J. Tarcha, Formation of selenium colloids using sodium ascorbate as the reducing agent, J. Colloid Interface Sci. **170**, 254 (1995).

[22] J. A. Johnson, M.-L. Saboungi, P. Thiyagarajan, R. Csencsits, and D. Meisel, Selenium nanoparticles: A small-angle neutron scattering study, J. Phys. Chem. B **103**, 59 (1999).

[23] H. Fan, Z. H. Wang, X. Z. Liu, W. W. Zheng, F. Guo, and Y. T. Qian, Controlled synthesis of trigonal selenium crystals with different morphologies, Solid State Commun. **135**, 319 (2005).

[24] S. Q. Lin, W. Li, Z. W. Chen, J. W. Shen, B. H. Ge, and Y. Z. Pei, Tellurium as a high-performance elemental thermoelectric, Nat. Commun. **7**, 10287 (2016).

[25] V. A. Shalygin, A. N. Sofronov, L. E. Vorob'ev, and I. I. Farbshtein, Current-induced spin polarization of holes in tellurium, Phys. Solid State **54**, 2362 (2012).

[26] V. A. Shalygin, M. D. Moldavskaya, S. N. Danilov, I. I. Farbshtein, and L. E. Golub, Circular photon drag effect in bulk tellurium, Phys. Rev. B **93**, 045207 (2016).

[27] C. Şahin, J. Rou, J. Ma, and D. A. Pesin, Pancharatnam-Berry phase and kinetic magnetoelectric effect in trigonal tellurium, Phys. Rev. B **97**, 205206 (2018).
[28] S. S. Tsirkin, P. A. Puente, and I. Souza, Gyrotropic effects in trigonal tellurium studied from first principles, Phys. Rev. B **97**, 035158 (2018).
[29] C. Patel, Optical Harmonic Generation in the Infrared using a CO_2 Laser, Phys. Rev. Lett. **16**, 613 (1966).
[30] S. Tutihasi and I. Chen, Optical properties and band structure of trigonal selenium, Phys. Rev. **158**, 623 (1967).
[31] G. G. Roberts, S. Tutihasi, and R. C. Keezer, Optical absorption edge of trigonal selenium, Phys. Rev. **166**, 637 (1968).
[32] G. W. Day, Linear and nonlinear optical properties of trigonal selenium, Appl. Phys. Lett. **18**, 347 (1971).
[33] J. McFee, G. Boyd, and P. Schmidt, Redetermination of the nonlinear optical coefficients of Te and GaAs by comparison with Ag_3SbS_3, Appl. Phys. Lett. **17**, 57 (1970).
[34] W. D. Teuchert, R. Geick, G. Landwehr, H. Wendel, and W. Weber, Lattice dynamics of trigonal selenium. I. Phonon spectra, J. Phys. C: Solid State Phys. **8**, 3725 (1975).
[35] R. Keller, W. B. Holzapfel, and H. Schulz, Effect of pressure on the atom positions in Se and Te, Phys. Rev. B **16**, 4404 (1977).
[36] K. Seifert, J. Hafner, J. Furthmüller, and G. Kresse, The influence of generalized gradient corrections to the LDA on predictions of structural phase stability: The Peierls distortion in As and Sb, J. Phys.: Condens. Matter **7**, 3683 (1995).
[37] J. P. Perdew, K. Burke, and M. Ernzerhof, Generalized Gradient Approximation Made Simple, Phys. Rev. Lett. **77**, 3865 (1996).
[38] P. E. Blöchl, Projector augmented-wave method, Phys. Rev. B **50**, 17953 (1994).
[39] G. Kresse and J. Furthmüller, Efficient iterative schemes for *ab initio* total-energy calculations using a plane-wave basis set, Phys. Rev. B **54**, 11169 (1996).
[40] G. Kresse and J. Furthmüller, Efficiency of *ab-initio* total energy calculations for metals and semiconductors using a plane-wave basis set, Comput. Mater. Sci. **6**, 15 (1996).
[41] P. E. Blöchl, O. Jepsen, and O. K. Andersen, Improved tetrahedron method for Brillouin-zone integrations, Phys. Rev. B **49**, 16223 (1994).
[42] G. Y. Guo and J. C. Lin, Systematic *ab initio* study of the optical properties of BN nanotubes, Phys. Rev. B **71**, 165402 (2005).
[43] B. Adolph, J. Furthmüller, and F. Bechstedt, Optical properties of semiconductors using projector-augmented waves, Phys. Rev. B **63**, 125108 (2001).
[44] V. B. Anzin, M. I. Eremets, Y. V. Kosichkin, A. I. Nadezhdinskii, and A. M. Shirokov, Measurement of the energy gap in tellurium under pressure, Phys. Status Solidi A **42**, 385 (1977).
[45] J. Heyd, G. E. Scuseria, and M. Ernzerhof, Hybrid functionals based on a screened Coulomb potential, J. Chem. Phys. **118**, 8207 (2003).
[46] Z. H. Levine and D. C. Allan, Quasiparticle calculation of the dielectric response of silicon and germanium, Phys. Rev. B **43**, 4187 (1991).
[47] E. D. Palik, *Handbook of Optical Constants of Solids II* (Academic, Orlando, 1985).
[48] R. Sandrock, Interpretation of the ultraviolet spectrum of trigonal selenium, Phys. Status Solidi B **43**, 199 (1971).
[49] P. Bammes, R. Klucker, E. E. Koch, and T. Tuomi, Anisotropy of the dielectric constants of trigonal selenium and tellurium between 3 and 30 eV, Phys. Status Solidi B **49**, 561 (1972).
[50] S. Tutihashi, G. G. Roberts, R. C. Keezer, and R. E. Drews, Optical properties of tellurium in the fundamental absorption region, Phys. Rev. **177**, 1143 (1969).
[51] H. Isomäki, J. Von Boehm, P. Krusius, and T. Stubb, Self-consistent electronic spectrum of trigonal Te: Pressure dependence of energy spectrum, Phys. Rev. B **22**, 2945 (1980).
[52] J. Treusch and R. Sandrock, Energy band structures of selenium and tellurium, Phys. Status Solidi B **16**, 487 (1966).
[53] J. Ingers, K. Maschke, and S. Proennecke, Optical-transition-matrix elements between localized electronic states in disordered one-dimensional systems, Phys. Rev. B **37**, 6105 (1988).
[54] J.-H. Song, A. J. Freeman, T. K. Bera, I. Chung, and M. G. Kanatzidis, First-principles prediction of an enhanced optical second-harmonic susceptibility of low-dimensional alkali-metal chalcogenides, Phys. Rev. B **79**, 245203 (2009).
[55] X. X. Jiang, S. G. Zhao, Z. S. Lin, J. H. Luo, P. D. Bristowe, X. G. Guan, and C. T. Chen, The role of dipole moment in determining the nonlinear optical behavior of materials: *Ab initio* studies on quaternary molybdenum tellurite crystals, J. Mater. Chem. C **2**, 530 (2014).
[56] A. Cammarata, W. G. Zhang, P. S. Halasyamani, and J. M. Rondinelli, Microscopic origins of optical second harmonic generation in noncentrosymmetric–nonpolar materials, Chem. Mater. **26**, 5773 (2014).